DEVELOPMENT AND CHARACTERIZATION OF NEWEST GENERATION HANDHELD SUNPHOTOMETER FOR MEASUREMENTS OF AEROSOL OPTICAL DEPTH BY CITIZEN SCIENTISTS

A Thesis
by
MATTHEW F. ALLEN

Submitted to the School of Graduate Studies
at Appalachian State University
in partial fulfillment of the requirements for the degree of
MASTER OF SCIENCE

December 2023
Department of Physics and Astronomy

DEVELOPMENT AND CHARACTERIZATION OF NEWEST GENERATION HANDHELD SUNPHOTOMETER FOR MEASUREMENTS OF AEROSOL OPTICAL DEPTH BY CITIZEN SCIENTISTS

A Thesis
by
MATTHEW F. ALLEN
December 2023

APPROVED BY:

_____
James Sherman, Ph.D.
Chairperson, Thesis Committee

_____
Christopher Thaxton, Ph.D.
Member, Thesis Committee

_____
Gregg Marland, Ph.D.
Member, Thesis Committee

_____
Tonya Coffey, Ph.D.
Chairperson, Department of Physics and Astronomy

_____
Ashley Colquitt, Ph.D.
Associate Vice Provost and Dean, Cratis D. Williams School of Graduate Studies

Abstract

DEVELOPMENT AND CHARACTERIZATION OF NEWEST GENERATION HANDHELD SUNPHOTOMETER FOR MEASUREMENTS OF AEROSOL OPTICAL DEPTH BY CITIZEN SCIENTISTS

Matthew Allen
B.S., Appalachian State University
M.S., Appalachian State University

Chairperson: Dr. James Sherman

Aerosol optical depth (AOD), a key aerosol property used in climate models and air quality studies, is primarily measured by satellite-based instruments such as NASA's Moderate Resolution Imaging Spectroradiometer (MODIS) and NASA's Multi-angle Imaging SpectroRadiometer (MISR). These satellite-based measurements, however, have higher uncertainties over complex, mountainous terrain. Due to these geographically dependent uncertainties, it is imperative to validate the satellite data with measurements from ground-based instruments such as NASA's Aerosol Robotic Network (AERONET), but spatial coverage over mountainous terrain within the United States and Africa, for example, is sparse. Networks of inexpensive handheld sunphotometers have the unique potential to complement AERONET and increase the spatial coverage of AOD measurements, but the usefulness of these measurements is heavily dependent on instrument design, adequate calibration, and characterization of instrument performance against reference standards such as the CIMEL sunphotometers used at AERONET sites. Dr. James Sherman's research group at Appalachian State University previously developed handheld microcontroller-based sunphotometers utilizing filtered photodiodes, which were deployed to Botswana in 2018 for Citizen Scientist AOD measurements. These instruments demonstrated excellent agreement with AERONET-measured AOD and long-term calibration stability but were restricted by issues related to time synchronization, data transmission,

reliability, and ease of use. I have designed and implemented software and hardware solutions to address these issues, including a new Global Positioning System (GPS) module to better synchronize the instrument's time and a new measurement protocol to optimize data acquisition. In addition, I have built upon previous students' work to improve the instrument's troubleshooting simplicity and to develop an improved housing to accommodate the instrument's new hardware components. Our newest generation handheld sunphotometer demonstrated excellent agreement in the initial comparisons with the CIMEL sunphotometer at Appalachian State's AERONET site, in addition to greatly improved functionality, reliability, and ease of use.

Acknowledgements

This research was financially supported by an NC Space Grant Graduate Fellowship award from the U.S. National Aeronautics and Space Administration and a Student and Faculty Excellence (SAFE) grant. Thank you to the faculty and staff at Appalachian State University who provided support during my academic career, including Dr. Sherman, Dr. Thaxton, Dr. Marland, Patrick Richardson, and Isaac Critcher.

Table of Contents

Chapter 1: Introduction

Atmospheric Aerosol Sources and Types

Aerosols, often observed as haze, dust, or smoke, are solid and liquid particles suspended in Earth's atmosphere. Aerosols can have profound effects on air quality, visibility, and Earth's energy budget. These airborne particles are highly diverse in their chemical composition and size distribution due to their numerous sources of origination and various formation methods (Myhre et al., 2013). Due to their relatively short atmospheric lifetimes, the effects of aerosols are primarily on regional scales. Approximately 90% of the global aerosol mass originates from natural sources, while the remaining 10% is considered anthropogenic (Voiland, 2010). However, anthropogenic aerosols can dominate near and downwind of urban/industrial sources. Particle sizes range from a few nanometers to tens of microns in diameter, influenced primarily by origination and atmospheric processing (Voiland, 2010).

Desert dust is the most globally prevalent aerosol type, followed by sea salt. Both of these aerosol types consist primarily of large particles with diameters larger than a micron. Wildfires, especially in the western United States, are an increasingly significant source of black carbon and organic aerosols (Wilmot et al., 2022). Major volcanic eruptions are another well-documented source of natural atmospheric aerosols. The smallest volcanic ash and dust particles can stay in the stratosphere on the order of months, while the sulfuric acid haze stemming from the sulfur dioxide emitted by erupting volcanoes can remain in the stratosphere for years (Kirk-Davidoff, 2018).

While only representing 10% of global aerosols by mass, anthropogenic aerosols are significantly abundant in and downwind of urban/industrialized regions, such as much of the

eastern United States. Most anthropogenic particles are smaller than one micron: (1) sulfates from the oxidation of power plant SO_2 emissions; (2) organic aerosols from the oxidation of tree emissions mediated by anthropogenic emissions; and (3) black carbon and organic aerosols emitted directly from combustion of fuels. Sulfate aerosol concentrations have decreased significantly in the eastern U.S. in the past few decades due to reduced emissions from coal-burning power plants as a result of the Title IV amendments to the Clean Air Act (Hand et al., 2020).

Since the physical size of particulate matter in the atmosphere is closely tied to the source of origination and radiative impact, aerosols are often classified based on their approximate size. These categories consist of the nucleation mode (1 to 10 nm), the Aitken mode (10 to 100 nm), the accumulation mode (100 nm to 1 μm), and the coarse mode (greater than 1 μm). Particles can be injected directly into the atmosphere from a wide variety of sources, including fossil fuel combustion, desert dust, and biomass burning. Nucleation mode particles are also produced through gas-to-particle conversion of precursor gasses. These smaller particles can grow to different modes throughout their atmospheric lifetime. Particles from the coarse mode, on the other hand, are mostly mechanically generated and originate primarily from natural sources. Particles in the atmosphere begin to act as cloud condensation nuclei (CCN) and begin to play a role in indirect climate forcing once they reach approximately 100 nm in diameter, while the most effective size range for direct climate forcing is around 400 to 700 nm (Pryor et al., 2015).

Aerosol Effects on Solar Radiation

Aerosols scatter and absorb sunlight, directly affecting Earth's energy budget. Aerosols also indirectly modify shortwave and longwave radiation through their complex interactions with clouds. Natural and anthropogenic aerosols can both serve as cloud condensation nuclei. Cloud

condensation nuclei serve as surfaces upon which tropospheric water vapor can condense to begin the formation of a cloud. Differences in CCN size, which is strongly correlated to the aerosol's source of origination, and CCN abundance impact cloud albedo, cloud lifetime, and precipitation efficiency (IPCC, 2023; Twomey, 1974). According to the latest Intergovernmental Panel on Climate Change Assessment (IPCC, 2023), the aerosol indirect and direct radiative effects represent the largest uncertainties on Earth's radiative forcing.

The aerosol Indirect Radiative Effect (IRE) and Direct Radiative Effect (DRE) represent the changes in the net downwelling solar flux (units: W/m^2) at either the top of the atmosphere or at the surface due to the presence of aerosols. Aerosol DRE is always negative at the surface, corresponding to less down-welling flux due to the presence of aerosols and leading to a cooling effect. DRE is usually negative at the top of the atmosphere, but its sign depends on whether aerosols increase or decrease the planetary albedo. Brighter aerosols over a darker surface increase the planetary albedo and result in a negative DRE, while darker aerosols (such as soot) over a brighter surface decrease the planetary albedo, leading to positive DRE at the top of the atmosphere (IPCC, 2023). Effective Radiative Forcing (ERF) is a relatively modern framework for comprehensively evaluating the strength of climate drivers with respect to radiative impact since 1750 (units: W/m^2). The globally averaged ERF due to aerosol-cloud interactions is currently estimated by the IPCC at around -1.0 [-1.7 to -0.3] W/m^2, while the ERF due to aerosol-radiation interactions is estimated at around -0.3 [-0.6 to 0.0] W/m^2 (IPCC, 2023), although the values vary greatly by region.

Calculations of aerosol radiative effects require knowledge of several aerosol optical properties, which are measured by satellite and ground-based networks: (1) Aerosol Optical Depth (AOD), the vertical integral of aerosol light extinction coefficient; (2) Single Scattering

Albedo (SSA), the fraction of light extinction due to scattering ($0 \leq SSA \leq 1$); and (3) aerosol size distribution, often estimated using the wavelength dependence of light extinction (AOD Angstrom exponent), along with the wavelength-dependence surface reflectance. Aerosol DRE is most sensitive to AOD, followed by SSA (Sherman & McComiskey, 2018). Mid-visible AOD in the rural southeastern U.S. typically ranges from less than 0.05 during winter to 0.20-0.30 in summer, with higher values occasionally observed from the long-distance transport of smoke and Saharan dust. SSA is a measure of the relative contributions of scattering and absorption to aerosol light extinction. Visible SSA is typically ~0.90-0.95 in the southeastern U.S., corresponding to bright, highly reflective aerosols. Values lower than this correspond to darker aerosols containing black carbon and are observed in regions with large amounts of biomass burning, such as South America and parts of sub-Saharan Africa. The AOD Angstrom exponent (AE) is the derivative of ln(AOD) with respect to ln(wavelength) and yields semi-quantitative information on average particle size. The AE can range from 0-4, with the smallest values corresponding to large particles (dust) and larger values corresponding to very small particles.

Instruments and Techniques Used for Measuring AOD

Aerosol optical depth (AOD) is an optical measurement of aerosol impact in an atmospheric column and is used both for quantifying aerosol radiative effects and air quality studies, such as global mapping of PM2.5 (surface particulate matter less than 2.5 microns in diameter) from space. Satellite-based instruments such as the Moderate Resolution Imaging Spectroradiometer (MODIS), located on NASA's Terra and Aqua satellites, and the Multi-angle Imaging SpectroRadiometer (MISR) instrument on NASA's Terra satellite, retrieve AOD at several visible and near-IR wavelengths, based on reflected solar radiance from the atmosphere under clear-sky conditions. MODIS is able to map global AOD approximately daily due to its

larger swath width, while MISR maps global AOD every 7-8 days. Both MODIS and MISR AOD measurements are capable of reasonable accuracy (ΔAOD ~0.05) over dark, homogeneous terrain, but these retrievals are complicated over highly inhomogeneous or bright terrain, such as mountains, deserts, and snow-covered surfaces.

Unlike the spectroradiometers utilized by satellite-based instruments, ground-based AOD measurements are typically made by sunphotometers, which derive AOD from directly transmitted solar radiance. These measurements are commonly used to gain a more detailed understanding of the presence of atmospheric constituents such as aerosols, water vapor, and ozone. NASA's Aerosol Robotic Network (AERONET) consists of automated CIMEL sunphotometers deployed at hundreds of global locations (Holben et al., 1998). With low AOD uncertainty of ~0.01-0.02 (Eck et al., 1999), AERONET serves as the 'gold standard' for AOD measurements and has been used in numerous regional and global 'ground-truth' evaluations of satellite-measured AOD (Levy et al., 2010; Sherman et al., 2016). However, many global regions, such as Africa and some mountainous U.S. regions, have large spatial gaps in AERONET sites (or no sites at all). The GLOBE network (Brooks & Mims, 2001) and others have attempted to increase ground-based spatial coverage of AOD with measurements made by Citizen Scientists using custom-built, inexpensive, handheld sunphotometers. Such networks offer great potential, but the scientific utility of Citizen Scientist measurements depends on the measurement accuracy, which must be determined via detailed inter-comparisons with co-located AERONET AOD measurements.

Sherman et al. (manuscript in progress) conducted an 11-year intercomparison of AOD measured by handheld sunphotometers constructed at Appalachian State University with that measured by Appalachian State's AERONET site. They found that with regular calibration, the

handheld sunphotometers were able to measure AOD to within ~0.01 of AERONET, with high correlation. To the best of Dr. Sherman's research team's knowledge, this represents the first long-term, detailed handheld sunphotometer inter-comparison with AERONET. A few of the Appalachian State handheld sunphotometers were deployed to Botswana International University of Science and Technology (BIUST) in 2018 and were used as part of the first full-year study of air quality in the region (Lassman et al., 2020). Included in the instruments used at BIUST were first-generation, semi-automated sunphotometers constructed at Appalachian State (Krintz, MS thesis), which used an Arduino microcontroller interface designed to simplify data-taking and data logging. The semi-automated sunphotometers also demonstrated similar AOD agreement with AERONET, but problems involving time synchronization, data transfer protocols, and other ease-of-use issues were identified. These issues necessitated design modifications before the instruments could be widely used by Citizen Scientists.

Objectives and Significance

The overarching research objective of this project is to sustain and expand upon long-term atmospheric measurements of AOD made by Citizen Scientist collaborators at universities in mountainous locations in the U.S. and Africa. The primary objectives of my research are to (1) improve our sunphotometer instrument's reliability and functionality so that the instruments are better suited for long-term Citizen Scientist measurements and (2) conduct an initial characterization of the newest generation handheld sunphotometer measurement uncertainties of the new-generation instrument. Specifically, I design and implement software and hardware solutions to address the previously discussed issues. I also field-test and calibrate the newest generation sunphotometer at ASU's NASA AERONET site in order to conduct an initial analysis of AOD measurement uncertainty.

Due to the gaps in ground based AOD instrument coverage that exist in some regions of Africa, handheld sunphotometers have the unique potential to increase spatial coverage of AOD validation sites. Improved instrument reliability and functionality will sustain and expand our North American and Sub-Saharan Mountain Aerosol Network (NASAMAN) of Citizen Scientists and contribute to closing the gap of ground based AOD instrument coverage (Lassman et al., 2020).

Thesis Structure

In this thesis, I discuss the methodology used to measure AOD with this type of handheld sunphotometer, including the instrument calibration process, calculation of AOD through the modification of the Beer-Lambert-Bouguer equation, and data processing software. I then overview the newest generation handheld sunphotometer's technical design, both hardware and software. After discussing my instrument modifications and the reasoning behind each modification, I explain the process and results of testing the functionality of the alterations. This is followed by an initial evaluation of the instrument's uncertainty. Lastly, I conclude with a discussion of my instrument calibration results and initial data comparison with AERONET.

Chapter 2: AOD Measurement Methodology

Inversion of Sunphotometer Measurements to Calculate AOD

Our microcontroller-based sunphotometers utilize four filtered photodiodes as detectors, with bandpass centered at 440 nm (violet/blue wavelength), 550 nm (green wavelength), 870 nm (near-infrared wavelength), and 940 nm (near-infrared wavelength). When the instrument is pointed directly at the sun, each photodiode produces a voltage [V] proportional to the solar irradiance received at the Earth's surface, which is given by a modified form of the Beer-Lambert-Bouguer equation (Brooks & Mims, 2001):

$$V - V_{!"\#\$} = \frac{\%!}{\_\_}\ell^{\blacksquare}C^{*+} \qquad \textbf{Equation 1}$$

The variables in Equation 1 are as follows: (1) the dark voltage [V_{dark}] is due to the small amount of current produced by the photodiode in the absence of light and must be subtracted from each measurement's total voltage; (2) the top-of-atmosphere voltage [V_0] that the photodiode would produce at the top of atmosphere is obtained from instrument calibration (section 2.2); (3) the relative air mass

$$m = \frac{\_\_}{-./(-12"\#\ 4245"6.1/\ "/724)} \qquad \textbf{Equation 2}$$

takes into account the decreased solar transmission due to longer atmospheric path length for solar elevation angles closer to the horizon (Young, 1994); (4) the normalized Earth-to-Sun distance

$$R = \frac{\_\_\_\_\_}{(\_^{\blacksquare}9.9,;<\ ")} \qquad \textbf{Equation 3}$$

$$,=9.9,;<*>1\text{-}(?@*+*A/C;D)$$

takes into account ellipticity of earth's orbit; and (5) the optical depth (OD) is a dimensionless,

wavelength-dependent measure of solar radiation attenuation by Earth's atmosphere, with the

atmosphere being more opaque to shorter wavelengths than to longer wavelengths. The optical depth includes the contributions due to Rayleigh scattering [$OD_{rayleigh}$] of incoming solar radiation by "clean air" molecules (such as nitrogen, oxygen, and carbon dioxide), absorption of incoming solar radiation by trace atmospheric gasses such as ozone [OD_{O3}], nitrogen dioxide [OD_{NO2}], and water vapor [OD_{H2O}], scattering and absorption of solar radiation due to clouds [OD_{Clouds}], and scattering and absorption of solar radiation due to atmospheric aerosols [AOD]. In terms of the individual contributions to OD, Equation 1 can be rewritten as

$$V - V_{dark} = \frac{V_0}{R^2} e^{-m*(OD_{rayleigh}+OD_{O3}+OD_{NO2}+OD_{H20}+OD_{clouds}+AOD)} \qquad \textbf{Equation 4}$$

Equation 4 can be inverted to yield AOD.

$$AOD = \frac{\ln\left(\frac{V - V_{dark}}{V_0 / R^2}\right)}{-m} - OD_{rayleigh} - OD_{O3} - OD_{NO2} - OD_{H20} - OD_{clouds}$$

Equation 5

Using Equation 5 to find AOD necessitates knowledge or assumptions of the other contributions to OD at the altitude of the measurements. The contribution due to clouds [OD_{cloud}] is zero if no clouds are along the instrument's line of sight with the sun. The contribution due to Rayleigh scattering [$OD_{Rayleigh}$] can be calculated with knowledge of surface pressure or elevation of the measurement site (Bodhaine et al., 1999). The optical depth contributions relating to absorption due to atmospheric ozone [OD_{O3}] and nitrogen dioxide [OD_{NO2}] can be reasonably approximated by satellite data and averaged historical data for a given location. The contribution due to water vapor absorption [OD_{H20}] is negligible at visible wavelengths and for the 870 nm channel. However, it can be large and highly variable at 940 nm. In fact, this difference in absorption between the two near-infrared wavelengths makes it possible to derive precipitable water vapor (PWV), which is a measure of vertically integrated water vapor in the atmospheric column.

Sunphotometer Calibration

In order to use Equation 5 to calculate AOD, it is necessary to acquire a value for the instrument's measured voltage at the top-of-atmosphere [V_0] for each sunphotometer wavelength, using a technique called the Langley plot method (Shaw, 1983). Taking the natural logarithm of both sides of Equation 1 gives

$$ln\,(V - V_{0123}) = ln\,{}^{5^5}{}^{*}{}^{44}{}_{+} - m * OD \qquad \textbf{Equation 6}$$

The Langley method involves taking measurements over a range of relative air mass values [m=1/sin(solar elevation angle)] on a cloud-free morning and fit of the linear portion of $ln\,(V - V_{012})$ versus *m* for each wavelength except 940nm, from which negative OD is the slope and V_0 is obtained from the y-intercept. An example of this procedure can be seen in Figure 1. A constant value of total OD implies that atmospheric conditions change little over the measurement duration, a condition often met over 1-2 hour periods during early morning and stable weather regimes.

The best calibrations are obtained soon after sunrise when the solar angle is rapidly changing. This gives rise to a greater range of *m* values and better fits. Ideally, a calibration dataset will have a relative air mass deviation of at least 3- 4 from start to finish. Due to the fact that uncertainties associated with the top-of-atmosphere voltage [V_0]

Figure 1

440 nm Calibration Curve Using Newest Generation Handheld Sunphotometer on 5/21/2023

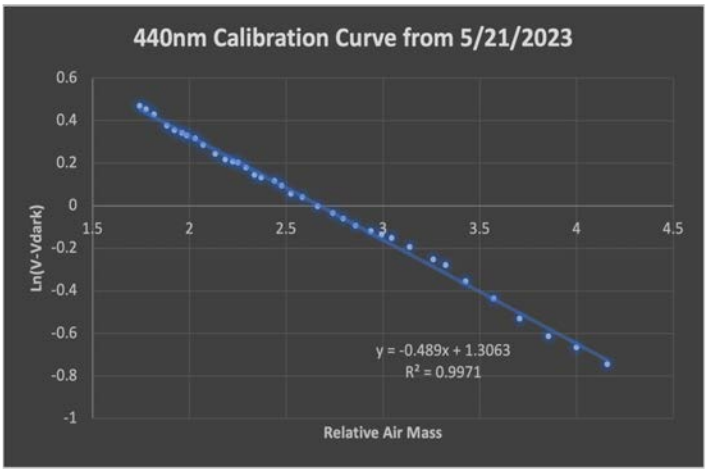

represent the instrument's largest AOD uncertainty (section 4.2), it is best practice to take the

mean or median V_o from several calibrations. Calibrations should be performed several times every year to mitigate the effect of long-term drifts in photodiode responsivity.

Data Collection, Archiving, and Processing

The process of routine sunphotometer data collection consists of taking triplets: three sequential measurement sets taken in a row. Each measurement comprising a triplet involves recording the maximum voltage at all four measured wavelengths, taken over a 13-second measurement window, along with a 2-second dark voltage measurement when the instrument is covered. Voltage variability greater than 1-2 % in the measurements comprising the triplet serves as an indicator of either poor instrument pointing during one or more measurements or thin clouds in/near the line of sight and can be used as a means of data quality assurance. Each individual measurement also includes additional variables for data processing: (1) a user-entered cloud code, indicating confidence in clear-sky conditions along the lines of site; (2) a temperature and pressure measurement made by sensors inside the sunphotometer; (3) sunphotometer battery voltage, along with date/time of measurement (for computing solar angle and for data analysis). The data is then saved as a CSV file onto the built-in SD card via the onboard Adafruit Data Logger (discussed in greater detail in Chapter 3). The data stored on the SD card is periodically uploaded to a laptop for archiving and processing.

The user-entered cloud code (Ian Krintz MS Thesis) is a simple yet effective method of logging the user's evaluation of the sky conditions at the time of the measurement. The presence of clouds in the atmosphere directly in between the sunphotometer and the sun will skew the instrument's measurements. Before each set of data collection, the user must input a cloud code of 0, 1, or 2. A value of 0 designates that the measurement is part of a calibration set. Data sets intended for calibration use also require clear sky conditions. A value of 1 indicates that the user

is confident that no cloud coverage obstructs the instrument's sightline of the sun. This includes thin cirrus clouds that are often difficult to see. Lastly, a value of 2 indicates that the user is not confident that there is an absolute absence of cloud coverage between the instrument and the sun.

Custom MATLAB code written by Professor Sherman is used for processing the triplet measurements and the calibrations. It includes functions for calculating the solar angle, Rayleigh optical depth, and linear regression analysis, in addition to several quality assurance tests. The code to process calibration data identifies the linear portions of Equation 6 and performs the fits from which the calibration constants V_0 are calculated for the 440 nm, 550 nm, and 870 nm sunphotometer channels. Calculated values V_o are only kept if all of the following conditions are met: (1) the linear portion of the curve (the data used for the calibration analysis) covers a wide enough range of relative air masses (default = 2.5) and includes a minimum number of data points (default =10); (2) the regression parameters satisfy minimum values for R^2 (default =0.90) and produce a regression slope which is consistent with the total optical depth expected for clear sky conditions. The program outputs plots of the calibration data and regression results, which are visually inspected as an additional quality assurance step. Values of V_0 from individual calibrations can sometimes pass all quality assurance tests yet produce poor AOD agreement with AERONET. We have found that taking the median V_0 of the nearest (in time) ~5 calibrations produces AOD that typically agrees with AERONET to within ~0.01-0.02.

The algorithm for processing triplet data is based on Equation 5 and includes quality assurance based on four primary components: (1) variability of the triplet measurements at each wavelength; (2) user-entered cloud code; (3) reasonable dark voltage values (typically 3mV or less); and (4) calculated AOD values that are physically reasonable. Triplet variability is typically indicative of either very faint clouds in or near the line of sight with the sun or poor

instrument pointing, in addition to small-scale turbulence (on windy days). Voltages within a given triplet typically do not vary by more than a few mV with optimized instrument sun-pointing and cloud-free conditions near the sun. Cloud code values of 2 are due to the uncertainty of potential thin clouds near the sun. Following an approach similar to AERONET (Holben et al., 1998), AOD measurements are classified by data quality level. Calculated AOD based on the raw measurements is classified as Level 1.0 and includes all measurements, regardless of whether they pass the quality assurance tests. Data passing the quality assurance tests are elevated to Level 1.5. This can be further modified only to include measurements with cloud codes of one if desired by the user. Level 2.0 data are the highest quality data and include re-processing of the Level 1.5 data, including time-interpolated values of V_o over an entire year and further cloud-checks. The Level 2.0 processing code is still being tested, so the data in this thesis is Level 1.5.

Chapter 3: Handheld Sunphotometer Instrument

Instrument Technical Design and Components

Our four-wavelength sunphotometers use four filtered photodiodes as detectors. A narrowband interference filter with a transmission bandwidth of ~10 nm is epoxied to each photodiode, with the filter's peak transmission wavelength defining the spectral channel. The 440 nm and 870 nm channels coincide with those of the CIMEL sunphotometers used by NASA AERONET, and the 550 nm channel coincides with the main wavelength used by MODIS to derive AOD. The shorter wavelengths are more sensitive to smaller particles, while the 870 nm channel is more sensitive to larger particles. The 940 nm channel coincides with a weak water vapor absorption band and can be used along with the 870 nm channel to derive precipitable water vapor. The calculation of precipitable water vapor is not yet incorporated into the data analysis software, so this 940nm data is not used within this thesis. The four photodiodes are mounted at the end of through holes made in a light-tight black optical block, which also maintains alignment of the photodiodes with the case apertures. The optical block also defines the detector's field of view so as to barely encompass the solar disk while still providing ease of alignment. The photodiode PCB and optical block can be seen in Figure 2. Two aligned sighting brackets mounted to the front exterior of the instrument case are used to optimize the instrument pointing at the sun.

Figure 2

Newest Generation Handheld Sunphotometer Components Including Filtered Photodiodes Soldered Into Their PCB (left) and Optical Block Housing (right)

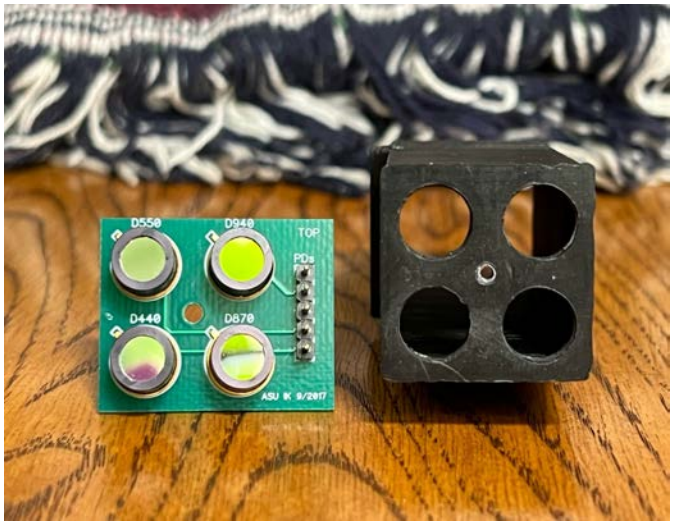

The photocurrents produced by the four photodiodes are converted to voltages using two dual op amps (LTC 1051) configured as trans-impedance amplifiers. The amplifier gain resistors are optimized separately for each channel to produce voltages of ~2-3 V during mid-day clear-sky conditions. The amplifier output voltages are digitized by a 16-bit analog-to-digital converter (Adafruit #4115) and stored by a data logger (Adafruit #2922), along with readings of pressure and instrument case temperature, which are measured by an Adafruit BME 280 sensor. The pressure measurement is used in the calculation of Rayleigh Optical Depth (Bodhaine et al., 1999), while the case temperature can be used to account for a small temperature dependence of the photodiode voltages. These components and their associated circuitry are all located on the instrument's main PCB (Figure 3).

The sunphotometer is controlled by an Adafruit Feather MO microcontroller (Adafruit Product ID: 3010), programmed using the Arduino C language. The Adafruit Ultimate GPS FeatherWing module (Adafruit Product ID: 3133) and Adalogger FeatherWing module (Adafruit Product ID: 2922) connect to the Feather M0 microcontroller via stacking headers. Utilizing the external antenna on the outside of the instrument housing, the Adafruit Ultimate GPS FeatherWing reads National Marine Electronics Association (NMEA) sentences to gather data such as latitude, longitude, altitude, date, and time. The GPS module repeatedly scans for NMEA

Figure 3

Newest Generation Handheld Sunphotometer Main PCB With Microcontroller, Data Logger, and GPS Module Mounted on Underside

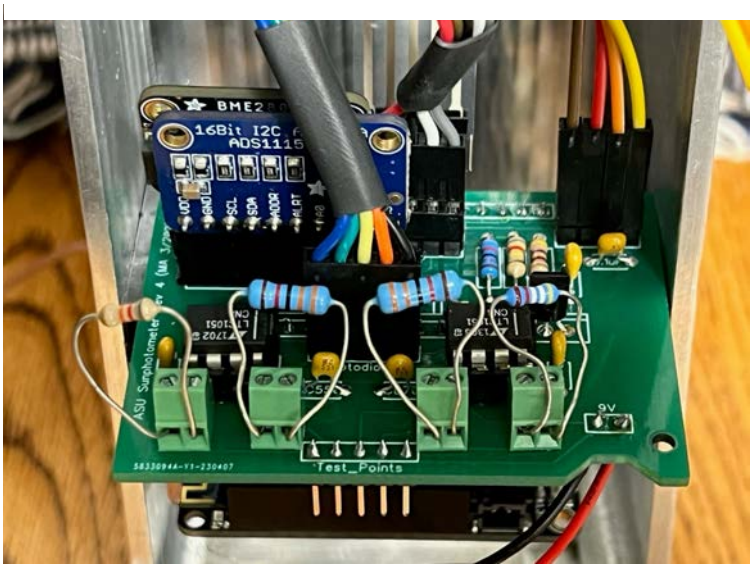

sentences and transfers the information to the microcontroller via serial communication pins (RX and TX). The GPS data, along with the BME 280 outputs, photodiode voltages, cloud code, and battery voltage, are transferred from the microcontroller to the Adafruit Adalogger FeatherWing using Serial Peripheral Interface (SPI) protocol. The data are continuously compiled onto a CSV file and saved to a micro-SD card within the datalogger. This removable micro-SD card is used to transfer the data to a PC for quality assurance and data processing.

State Machine Procedure

Our handheld sunphotometer instrument is programmatically controlled by a Mealy algorithmic state machine (ASM) written in C++ within the Arduino Integrated Development Environment (IDE). This state machine is designed to be heavily automated with minimal input required from the user in order to maximize ease of use and facilitate participation from Citizen Scientists in the data acquisition process. The ASM chart mapping our software functionality can be seen in Figure 4. When the sunphotometer is powered on via the main pushbutton switch, the state machine begins in the “Initialize” state. Here, the microcontroller reads the date and time from the GPS module and attempts to establish connectivity with the various sensors, the LCD screen, and the analog-to-digital converter (ADC). If there are initialization errors with any components, the system enters the “Fault” state and provides the user with a feedback message describing the present error in order to assist in troubleshooting. Otherwise, the state machine enters the “Idle” state.

While in the “Idle” state, the screen displays the current cloud code and the GPS date and time. The cloud code can be toggled by the user while the GPS date and time continue to update until the measure button is pressed, prompting the state machine to enter the “Dark Voltage Measurement" state. Within the “Dark Voltage Measurement” state, the sunphotometer begins to

sequentially measure the voltage produced by each of the four photodiodes when not pointed at the sun. During this state, which loops for approximately two seconds, the minimum voltage variable corresponding to each of the four photodiode wavelengths is systematically overwritten until each of the four variables contains the minimum measured voltage of their respective photodiode over the interval. After all four channels have been measured, the “Dark Measurement Loop” number is incremented, and the state continues to loop until the designated 16-loop limit has been reached. This state loops 16 times to ensure a 2-second time interval for gathering dark voltages. During this interval, the user covers the photodiode opening in order to acquire the dark voltage for each wavelength, as discussed in Chapter 2. The state machine proceeds to the “Light Measurement" state after the previous two-second interval expires, at which time the user points the instrument at the sun and uses the sunspot transmitted through the instrument sighting bracket to optimize instrument pointing. During the “Light Measurement” state, which loops for 13 seconds, the maximum voltage corresponding to each of the four photodiode wavelengths is systematically overwritten until each of the four variables contains the maximum measured voltage of their respective photodiode over the interval. After all four channels have been measured, the “Light Measurement Loop” number is incremented, and the state continues to loop until the designated 84-loop limit has been reached. This state loops 84 times to ensure a 13-second light interval for gathering light voltages. After this interval ends, the state machine proceeds to save the relevant data to the data logger’s SD card. Here, the recorded date, time, pressure, instrument case temperature, minimum dark voltages for each channel, maximum light voltages for each channel, cloud code, and battery voltage are all saved to the instrument’s continuous CSV file on the onboard SD card. The state machine then returns to the “Idle” state.

Figure 4

Mealy Algorithmic State Machine Chart Outlining the Microcontroller Code for the Newest Generation Handheld Sunphotometer's State Machine

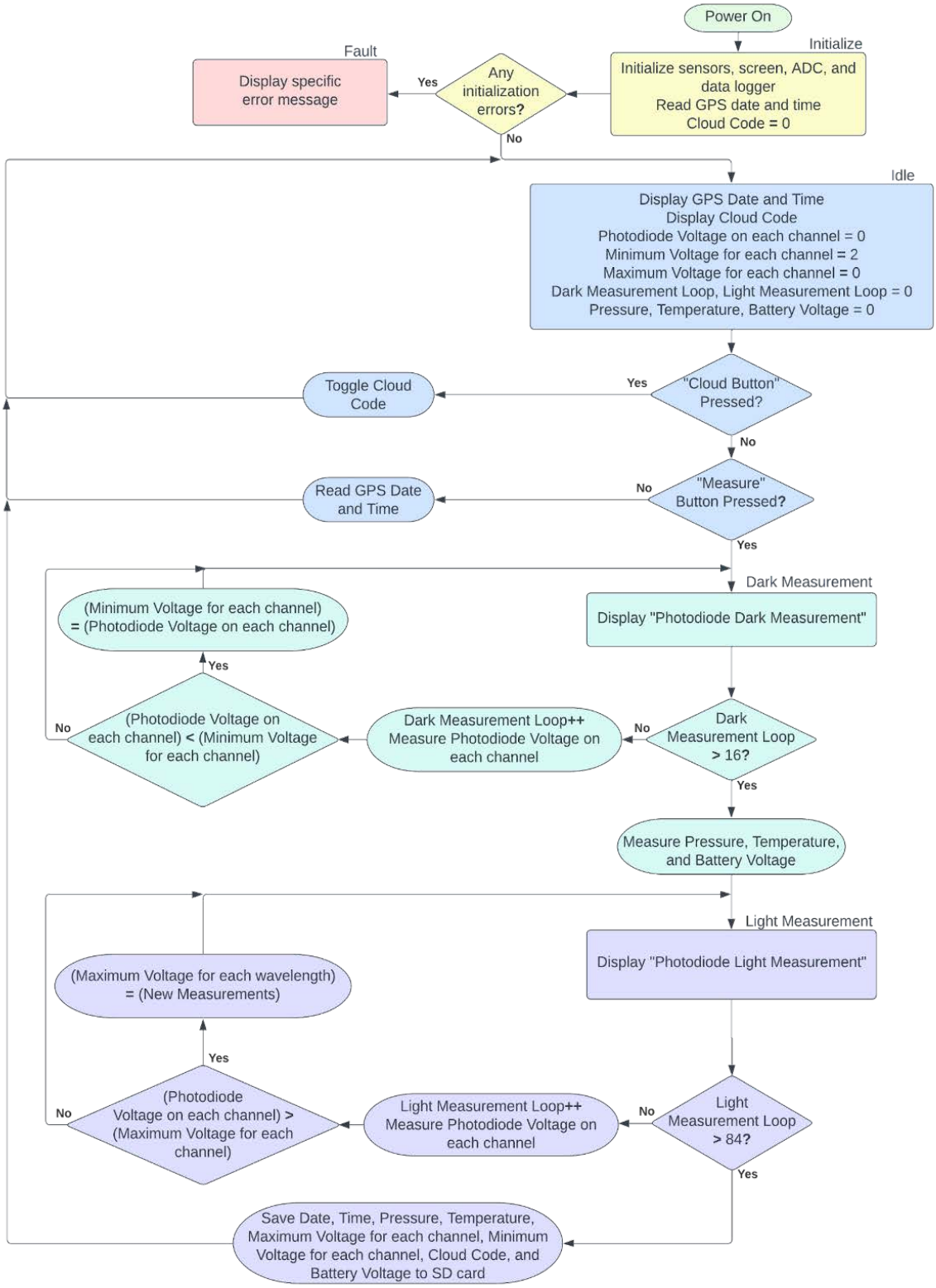

Newest Generation Instrument Modifications

The primary modifications I implemented to improve the previous generation instrument were necessary to address issues involving the sunphotometer's real-time clock (RTC), wireless data transfer, and data acquisition process. Additionally, the hardware alterations I introduced necessitated a redesign of the instrument's housing (Appendix A) and the primary circuit board (Appendix B).

Our previous generation sunphotometer utilized the Adafruit Feather M0 microcontroller's WIFI capabilities to query public web-based time servers in conjunction with the onboard RTC in an attempt to acquire the correct Coordinated Universal Time (UTC) consistently. When the previous-generation instruments were deployed in Botswana, the WIFI-based RTC method of keeping time proved to be particularly unreliable. To address this, I integrated an Adafruit Ultimate GPS FeatherWing module. The GPS module receives updated satellite data every second, eliminating the instrument's reliance on consistent WIFI access. This new method of keeping time is not subject to the possibility of time-drift complications commonly associated with many commercially available real-time clocks.

The Adafruit Ultimate GPS FeatherWing is a low-power GPS module that features an update rate of 10 Hz, which far surpasses the 1 Hz update rate requirement for the timekeeping role of this application. The integration of this new GPS module necessitated some changes to the instrument housing and main circuit board design. The previous RTC module connected to the microcontroller via the main circuit board while the Ultimate GPS module physically plugs into the microcontroller, along with the data logger. I removed the old RTC connection points on the main circuit board in order to make room for the new precision amplifier test points that I added to improve the system's ease of troubleshooting. These test points are additional header

pins that are connected to the traces of each of the four precision amplifier outputs. With these new test points, the user can attach jumper wires to the header pins and, while the instrument is pointed towards the sun, directly read the amplified photodiode voltage of each channel before the values are digitized by the ADC and recorded to the SD card via the data logger. If any issues arise regarding the photodiode voltage values in the spreadsheet, the inclusion of these test points provides a method of verifying that the photodiodes and op-amps are performing as expected. I also slightly extended the height of the instrument's housing to accommodate the vertical footprint of the new GPS module while still enabling handheld instrument operation.

Previously, the reliability of the instrument's WIFI connectivity also introduced complications with the data transfer process. The previous instrument stored all data on the onboard SD card and, when prompted, utilized a WIFI connection to transfer all the data onto a PC for data processing. To eliminate the WIFI dependency of the instrument, I altered the microcontroller code to remove the wireless data transfer functionality and reverted back to the method of physically removing the SD card to transfer data to a PC for processing. This simple solution allowed me to use the existing data storage infrastructure while totally eliminating a primary source of unreliability associated with the previous generation instrument. This alteration also necessitated a slight increase in the size of the access point in the instrument housing's sidewall to allow for easy SD card removal.

The instrument's previous software design used a data acquisition process that separated all the voltage measurements of each photodiode into sequential intervals. Essentially, during the "Light Measurement" state mentioned above, the old design would have the microcontroller repeatedly overwrite the maximum photodiode voltage variable for one wavelength until the user was satisfied with the value. After the user felt that they had stored the highest achievable

voltage, they would prompt the instrument to continue the same process for the next wavelength. This method introduces a few unnecessary sources of inaccuracy. First and foremost, each data entry row within the CSV file stored on the instrument's SD card has a single time stamp that applies to all eight photodiode voltage measurements, consisting of a light and a dark voltage measurement at each of the four wavelengths. The old data acquisition method allowed for the possibility of a much greater time deviation if the measurement of the first wavelength was significantly before the last wavelength's measurement. This new data acquisition process ensures that all voltage measurements occur within 15 seconds of the corresponding time stamp, which provides a more accurate representation of the current solar angle and resulting relative air mass. In section 4.2, I discuss the impact of this 15-second measurement window on the instrument's AOD measurement uncertainty.

Chapter 4: Results and Discussion

Testing the Sunphotometer Hardware Modifications

Prior to the data acquisition phase of this project, it was necessary to evaluate the various instrument modifications. Through serial port monitoring and repetitive data collection, I performed functionality testing throughout the instrument development phase to ensure that all of my alterations were performing as expected. After initial testing of our newest generation sunphotometer's modifications, my hardware and software modifications have proven to be promising.

The newly implemented Adafruit Ultimate GPS FeatherWing module has proven to be a significantly more effective method of keeping time than the previous RTC module. In addition to partially eliminating the instrument's previous reliance on a strong WIFI connection, the GPS module has shown that it is particularly reliable at maintaining a constant satellite connection in order to provide an accurate time and date without the clock drift associated with most commercially available RTCs. Since the accuracy of the timekeeping is easily verified using an online UTC clock, I determined that the instrument's time never deviated from the online UTC clock by more than 1 second after the GPS module secured a solid satellite connection. Throughout my preliminary testing, the GPS module consistently required about 30 seconds to establish a strong satellite connection initially. While the GPS module has worked reliably and consistently in North Carolina, further testing is required to guarantee the same effectiveness in other locations, such as Sub-Saharan Africa. The GPS module implementation also allows for the inclusion of the available latitude, longitude, and elevation data, if necessary, for future instrument generations.

Through repetitive measurements, I determined that my modification of the microcontroller software to remove the wireless data transfer functionality was successful. The instrument now saves each data set to the onboard SD card without attempting to transfer the data to a designated computer through a WIFI connection. The 4GB micro-SD card currently utilized by the newest generation sunphotometer can hold an estimated 29,000,000 measurement entries (rows) within the CSV file. This micro-SD card could be easily and inexpensively replaced by one with more memory if this became necessary in the future. This modification completes the process of entirely eliminating the instrument's reliance on WIFI. Throughout my entire testing process, this modification did not present any complications. The straightforward housing modification that I implemented to accommodate this data transfer alteration, relocating and increasing the size of an access point in the side of the housing to allow for the physical removal of the micro-SD card, also has proved to be effective.

Through standard data collection and microcontroller serial port monitoring, I have determined that the new iterative looping method of photodiode voltage measurement (section 3.2) works as designed. The minimum and maximum values are being overwritten correctly, and the four photodiode channels are being appropriately cycled through with every measurement loop. Based on the microcontroller serial port timestamps, I have also determined that the variation in the time duration for each measurement cycle is negligible, which validates the success of using a set number of measurement loops in order to achieve a 15-second total measurement window.

The implementation of the instrument's new main circuit board design and assembly has not resulted in any complications. The new circuit board design only differed from the previous design in regard to slight physical size adjustments, the removal of the previous RTC circuitry,

and the addition of test points on the four outputs of the trans-impedance amplifiers. Neither the physical size adjustments nor the removal of the old RTC has affected the instrument's functionality or accuracy. The new test points on the LTC 1051 outputs aid troubleshooting in the event of improper instrument performance in the future. This addition will allow a user to easily and directly measure the amplified photodiode voltages of all four channels that are recorded by the datalogger after being processed by the 16-bit ADC.

Calibration Results

As discussed in section 2.2, instrument calibration datasets are acquired on clear, still mornings over the course of at least an hour to provide a stable regression slope (-OD) over a wide range of relative air mass values. These conditions offer the best chance for the calibration curve to yield an accurate y-intercept and resulting V_0 value. Weather conditions over the course of the data acquisition period allowed for a few calibration datasets to be collected. I was able to collect four usable datasets for the 440 nm channel and three usable datasets for the 550 nm and 870 nm channels. I disqualified one of the calibration datasets for the 550 nm and 870 nm channels because the curve slopes were not constant enough to provide an acceptable coefficient of correlation. By taking the mean of the resulting V_0 values from all datasets for a given wavelength, I have calculated the newest generation handheld sunphotometer's V_0 values for each wavelength (Table 1). This table also contains the standard deviation of each wavelength's calibration voltage ΔV_0 for the purpose of the uncertainty analysis of each channel.

Table 1

Newest Generation Handheld Sunphotometer Mean V_0 Values and Standard Deviation of V_0 Values [ΔV_0] at Each Wavelength

	440nm	550nm	870nm
V_0	4.1027V	1.3964V	2.0987V
ΔV_0	0.0787V	0.0304V	0.0356V

Initial Zero Order AOD Uncertainty Analysis of Newest Generation Sunphotometer

The newest generation instrument zero order AOD uncertainty can be evaluated by adding the individual uncertainties relevant to the AOD calculation in quadrature since they are uncorrelated. This includes the uncertainties associated with calibration voltage V_0, measurement voltage V, and relative air mass *m*. By taking the partial derivatives of Equation 5 with respect to V_0, V, and *m*, we can determine the AOD sensitivity to each.

$$\frac{\partial AOD}{\partial Vo} = \frac{1}{mVo}$$

$$\frac{\partial AOD}{\partial V} = -\frac{1}{m(V - Vdark)}$$

$$\frac{\partial AOD}{\partial m} = \frac{ln(V - Vdark) - ln(Vo/R^5)}{m^5}$$

These sensitivities can be multiplied by their associated uncertainties and added in quadrature (Michalsky et al., 2001) to find the total instrument uncertainty

$$\Delta AOD = \sqrt{(\frac{678/78}{=})^5 + (\frac{67/(7<7=>?@)}{=})^5 + (\frac{6:(BC(7<7=>?@)<BC(78/D^!))}{=\ !})^5} \qquad \textbf{Equation 7}$$

As discussed in section 4.2, my estimates for the uncertainty of each wavelength's top-of-atmosphere voltages [ΔV_0] are the standard deviations of the V_0 values acquired through multiple instrument calibrations. The fractional uncertainty $\Delta V_0 / V_0$ used in Equation 7 is obtained simply by dividing ΔV_0 by the mean (or median) V_0 over several calibrations. The

fractional uncertainties of the instrument calibration voltages for the 440 nm, 550 nm, and 870 nm channels, expressed as percentages, are 1.92%, 2.18%, and 1.69%, respectively.

The measurement voltage uncertainty [ΔV] arises from two sources: (1) small deviations from the optimum instrument pointing at the sun and (2) the (weak) temperature dependence of photodiode voltage. A third source of uncertainty, equal to the least significant bit of the ADC, is negligible (0.076 mV) and is neglected in comparison to the other two sources. The uncertainty associated with instrument pointing inaccuracy can be estimated by optimizing instrument pointing using the sunspot transmitted through the instrument sighting bracket on a cloud-free day and then taking the standard deviation of voltages recorded over the 13-second measurement window. This window is short enough to avoid instrument heating from the sun so that the photodiode temperature variations are negligible. For the 440 nm channel, this procedure yielded a standard deviation of 9.7 mV with a mean voltage of 1.4740 V, resulting in a fractional uncertainty, expressed as a percentage, of approximately 0.66%.

The correction to photodiode voltages to account for small temperature dependence has not yet been incorporated into the data analysis software, but the magnitude of the uncertainty can be evaluated by taking repetitive measurements on a hot, cloud-free, and low-turbulence day around noon. The sunphotometer is first placed in a cool room before beginning measurements. The instrument is then taken outside and pointed at the sun, resulting in a continuous increase in instrument temperature. The instrument voltage is continuously optimized (due to the lack of a solar tracker) over a ~5-minute interval (over which solar angle changes negligibly near noon). During this time, maximum voltage and instrument temperature are continuously recorded. A plot of sunphotometer voltage versus instrument temperature is then made to quantify the temperature sensitivity. This simplistic method on a given day can only estimate the temperature

dependence over a ~10°C range, but curves on summer and winter days can extend the coverage over the range of temperatures typical of the sunphotometer measurements. We observed a 4 mV increase in photodiode voltage at 440 nm over a temperature range of 10°C, leading to an average sensitivity of 0.4 mV per degree Celsius for a photodiode voltage output of approximately 1.0 V. The instrument temperature typically varies by, at most, 5°C over a given triplet, so we estimate the uncertainty in photodiode voltage at 440 nm to be 2.0 mV, with a fractional uncertainty ΔV/V=0.2%. The fractional pointing uncertainty and temperature drift uncertainty can be put in quadrature to calculate a final measurement voltage uncertainty for the 440 nm channel.

$$\frac{\Delta V}{(V - Vdark)} \; at \; 440\, nm \; = \; \frac{1}{\sqrt{\left(\frac{0.0097V_6}{1.4740V}\right) + \left(\frac{0.0020V_6}{1.0000V}\right)}} \; = \; 0.69\%$$

The measurement voltage fractional uncertainties for each wavelength are provided in Table 2.

Table 2

Newest Generation Handheld Sunphotometer Measurement Voltage Fractional Uncertainties for Each Wavelength

	440 nm	550 nm	870 nm
$\frac{\Delta V}{(V - Vdark)}$	0.0069	0.0113	0.0961

The uncertainty due to the relative air mass [Δm] can be found with a simple calculation evaluating the result of clock inaccuracy on the resulting relative air mass value. The solar elevation angle is most rapidly changing in the morning and evening, so using values from around 8:00:00 AM local standard time provides a reasonable upper bound uncertainty estimate. As discussed in Chapter 3, the instrument's measurement window lasts for 15 seconds. After acquiring a satellite fix, the GPS module does not deviate from online Universal Coordinated Time (UTC) clocks by more than 1 second. For an upper-bound estimate of relative air mass

uncertainty, we can use Equation 2 with solar elevation angles from 8:00:00 AM and 8:00:16

AM to find the difference between the resulting relative air mass values. At 8:00:00 AM on April 15th (same date as used in section 3.3 discussion), the relative air mass can be calculated as

$$m = \frac{1}{sin(28.96°)} = 2.065$$

At 8:00:16 AM on the same day, the resulting relative air mass is

$$m = \frac{1}{sin(29.01°)} = 2.062$$

This 0.003 difference in relative air mass values is this instrument's relative air mass uncertainty [Δm].

Inserting the various uncertainty variables for each wavelength into Equation 7 yields the following wavelength-dependent zero-order AOD uncertainty estimate for the prototype newest generation sunphotometer

$$\Delta AOD\ at\ 440\ nm = ?(\frac{3.3567}{*})^7 + (\frac{3.3386}{*})^7 + (\frac{3.339(!"(\$)\$/012))!"(\$:/\&")}{*"})^7 \qquad \textbf{Equation 8}$$

The dominant source of AOD uncertainty [ΔAOD] is the calibration voltage V_0, with a fractional uncertainty of 0.0192 for the 440 nm channel. The second most dominant source of AOD uncertainty is the measurement voltage with a fractional uncertainty of 0.0069 for the 440 nm channel. The relative air mass uncertainty, with the entire measurement window limited to 15 seconds, is significantly less than both other sources of uncertainty under the same conditions. While ΔAOD is dependent on multiple variables for each individual measurement, the newest generation handheld sunphotometer's AOD uncertainty is expected to be between 0.01 and 0.02 based on the evaluation of Equation 8 for all wavelengths using triplets values from my initial measurements.

Due to complex atmospheric and instrument sources, analytical equations such as those outlined above can only provide crude estimates of AOD uncertainty. Comparisons of

sunphotometer-derived AOD with that measured at a co-located or nearby AERONET site is the most accurate method of evaluating the quality of sunphotometer performance. By plotting sunphotometer-measured AOD versus AERONET AOD, the correlation between the data points can be analyzed to assess the instrument's performance. Generating an error envelope around the resulting regression line that encompasses a set percentage of the data points is a methodology used by prominent evaluations of AOD instrumentation (Gupta et al., 2018; Levy et al., 2010). The development of these error envelopes, however, requires a quantity of data points that far exceed the amount collected using our newest generation handheld sunphotometer within this thesis. Because of this, I instead compare the regression parameters generated by my AERONET comparison to the trendline from a recent MODIS-AERONET comparison (Gupta et al., 2018) from data isolated to the Eastern United States (section 4.4).

Comparison of Sunphotometer and AERONET-measured AOD

To evaluate the accuracy of our newest generation handheld sunphotometer's AOD measurements, I have plotted handheld sunphotometer-measured AOD values against AERONET's AOD collected at the same timestamp. This procedure required slight data manipulation to compare the sources accurately. AERONET does not measure AOD at 550 nm. The 550 nm photodiode selection for our handheld sunphotometer coincides with the primary AOD wavelength measured by MODIS (discussed in section 3.1). Therefore, I scaled AERONET AOD measured at 500 nm to 550 nm by performing an angstrom correction (Barman et al., 2019) using the AERONET-provided angstrom exponent for each triplet. Also, since AERONET measures AOD in 5-minute intervals (at best), I used a time-weighted interpolation between the nearest AERONET measurements on either side of each of my handheld sunphotometer measurements to correct for the timestamp differences to the best of my ability.

The AOD comparison scatter plots at 440 nm, 550 nm, and 870 nm can be seen in Figure 5, Figure 6, and Figure 7, respectively.

Figure 5

Newest Generation Handheld Sunphotometer AOD vs AERONET AOD Scatterplot Comparison at 440 nm With the Black Dotted Line Representing a One-to-One Line of Perfect Correlation

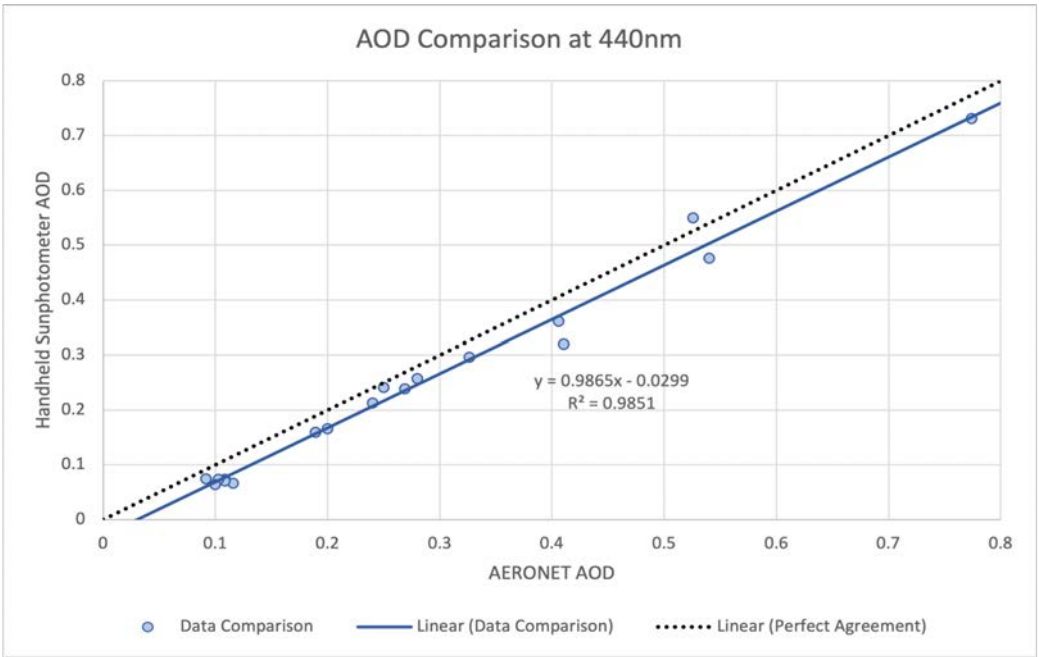

Figure 6

Newest Generation Handheld Sunphotometer AOD vs AERONET AOD Scatterplot Comparison at 550 nm With the Black Dotted Line Representing a One-to-One Line of Perfect Correlation

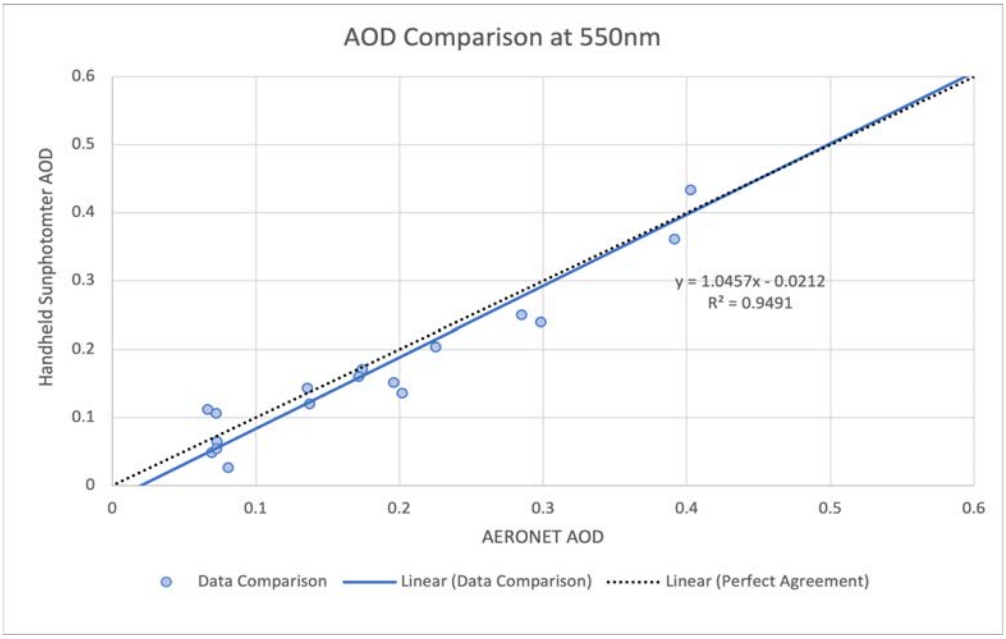

Figure 7

Newest Generation Handheld Sunphotometer AOD vs AERONET AOD Scatterplot Comparison at 870 nm With the Black Dotted Line Representing a One-to-One Line of Perfect Correlation

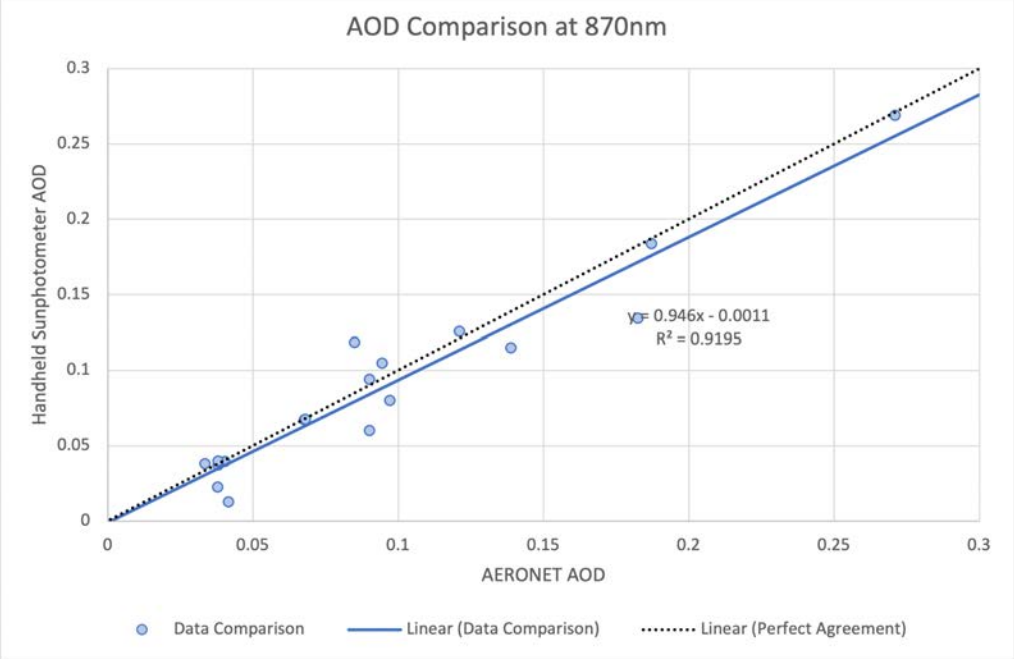

Following the data comparison technique of multiple prominent AERONET AOD comparison studies (Gupta et al., 2018; Levy et al., 2010), I have used my scatter plot trend lines to assess my instrument's agreement with AERONET-measured AOD. The results of this comparison can be seen in Table 3.

Table 3

Newest Generation Handheld Sunphotometer AOD vs AERONET AOD Data Comparison Results with MODIS 550nm AOD vs AERONET 550nm AOD for Context

	440nm	550nm	870nm	MODIS 550nm
Slope	0.9865	1.046	0.9460	1.22
Y-Intercept	-0.0299	-0.0212	-0.011	Not provided
R	0.9925	0.9742	0.9589	0.90
RMSE	0.0405	0.0363	0.0189	0.09
Mean bias	-0.0336	-0.0120	-0.0062	0.029

Columns 2, 3, and 4 of Table 3 represent the results from the data comparison of the handheld sunphotometer AOD and AERONET-measured AOD while the last column displays the same data from a recent study comparing MODIS-retrieved AOD at 550nm to AERONET-measured AOD at the same wavelength (Gupta et al., 2018). This MODIS-AERONET comparison utilizes 3km Dark Target AOD product data from both MODIS instruments (located on Aqua and Terra) and only includes top-quality assured data. This MODIS data set is isolated to include data from retrievals over the eastern half of the United States.

The initial data in Table 3 shows that the newest generation handheld sunphotometer is able to maintain a high level of agreement with AERONET-measured AOD. This data seems to indicate that handheld sunphotometers can possess sufficient accuracy for satellite AOD validations and for studies of air quality and aerosol direct radiative effects, as seen in other related studies (Sherman, manuscript in progress). Though my analysis included a very small quantity of data points compared to the MODIS-AERONET comparison, it is worth noting that the scatterplots for my instrument's 440nm, 550nm, and 870nm AOD measurements yielded a significantly better slope, correlation coefficient (R), and root mean square error than the MODIS comparison for the same geographic region. The MODIS data did have a slightly lower overall mean bias than my instrument's 440nm channel. This is likely due to imperfect calibration datasets and should improve with further data collection.

Chapter 5: Conclusions, Limitations, and Future Work

Conclusions

The results of my initial AOD data comparison between our new-generation handheld sunphotometer and AERONET have displayed a high level of agreement, on the order of ~0.02. This level of agreement is similar to that of an 11-year comparison with AERONET made by Sherman (manuscript in progress) using an earlier generation sunphotometer and suggests the capability for validating AOD retrieved by satellites and use in aerosol studies. While more data collection is required to better evaluate the accuracy of the newest generation handheld sunphotometer, the initial data results are promising.

The improved reliability, ease of troubleshooting, and ease of use modifications all have performed as designed and significantly enhanced the aspects of the instrument that I sought to address in order to facilitate more participation from Citizen Scientists in the future. The newly implemented GPS module has proven to be a reliable and highly accurate source of timekeeping without requiring a stable WIFI connection. The new automated measurement process simplifies the data acquisition procedure and guarantees a set timestamp inaccuracy. The new data transfer system has proven to be easy and reliable while entirely eliminating the instrument's reliance on WIFI. The first revision of the newest generation handheld sunphotometer has yielded overall promising results and can continue to be evaluated through further data collection in the near future.

Future Work

While initial testing of our newest generation handheld sunphotometer has yielded promising results in regard to greatly improved functionality, more data collection and analysis

are needed in order to characterize the quantitative impact of the new instrument modifications fully. Further data collection in the future will allow for the instrument to be more rigorously evaluated against AERONET. This continuation is necessary to comprehensively assess the utility of the instrument's data for the purpose of filling in spatial gaps in AERONET sites. Additional data collection by future students will also present more opportunities for any unnoticed software or hardware complications to emerge.

Since this instrument is the first revision of the new housing design, there is room for improvement in the next few that are constructed. The alignment of the optical block within the instrument's aluminum housing is imperfect. The physical fit of the optical block in its designated slot can be improved through the elimination of the rounded interconnection between the two. This initial design proved to be somewhat problematic during the machining process. The result of this imperfection is the slight misalignment of the sighting brackets on the front face of the outside housing. This does not necessarily negatively impact the instrument's accuracy, but it results in a slightly more inconvenient arrangement of the sighting bracket. The slight improvement of this housing design will make it easier to optimize the pointing angle of the instrument.

Due to differences in satellite global flight patterns, additional testing in other geographic regions is necessary to evaluate any significant differences in the instrument's GPS module viability in other countries. It remains to be determined whether the GPS module would be subject to a significant change in initialization time before syncing with nearby satellites if used in other regions of the world.

A rechargeable 9V lithium-ion battery with onboard USB charging capabilities could be easily incorporated into the system's design in the near future. This would prevent the user from

needing to remove the battery cover panel on the back of the instrument's housing to switch out the interchangeable 9V battery when necessary. This alteration could simply improve the ease of use of the instrument.

References

Barman, N., Roy, R., Saha, B., Kundu, S. S., Borgohain, A., De, B. K., & Guha, A. (2019). Investigation of seasonal variation of compensation parameter and absorption Ångström Exponent of aerosol after loading correction over a remote station in north-east India. *Atmospheric Environment*, *212*, 106–115. https://doi.org/10.1016/j.atmosenv.2019.05.036

Bodhaine, B. A., Wood, N. B., Dutton, E. G., & Slusser, J. R. (1999). On Rayleigh optical depth calculations. *Journal of Atmospheric and Oceanic Technology*, *16*(11), 1854–1861. https://doi.org/10.1175/1520-0426(1999)016<1854:ORODC>2.0.CO;2

Brooks, D. R., & Mims, F. M. (2001). Development of an inexpensive handheld LED-based Sun photometer for the GLOBE program. *Journal of Geophysical Research: Atmospheres*, *106*(D5), 4733–4740. https://doi.org/10.1029/2000jd900545

Eck, T. F., Holben, B. N., Reid, J. S., Dubovik, O., Smirnov, A., O'Neill, N. T., Slutsker, I., & Kinne, S. (1999). Wavelength dependence of the optical depth of biomass burning, urban, and desert dust aerosols. *Journal of Geophysical Research: Atmospheres*, 104(D24), 31333–31349. https://doi.org/10.1029/1999jd900923

Gupta, P., Remer, L. A., Levy, R. C., & Mattoo, S. (2018). Validation of MODIS 3 km land aerosol optical depth from NASA's EOS Terra and Aqua missions. *Atmospheric Measurement Techniques*, *11*(5), 3145–3159. https://doi.org/10.5194/amt-11-3145-2018

Hand, J. L., Prenni, A. J., Copeland, S., Schichtel, B. A., & Malm, W. C. (2020). Thirty years of the Clean Air Act Amendments: Impacts on haze in remote regions of the United States (1990–2018). *Atmospheric Environment*, *243*, 117865. https://doi.org/10.1016/j.atmosenv.2020.117865

Holben, B. N., Eck, T. F., Slutsker, I., Tanré, D., Buis, J. P., Setzer, A., Vermote, E., Reagan, J. A., Kaufman, Y. J., Nakajima, T., Lavenu, F., Jankowiak, I., & Smirnov, A. (1998). AERONET—A federated instrument network and data archive for aerosol characterization. *Remote Sensing of Environment*, *66*(1), 1–16. https://doi.org/10.1016/s0034-4257(98)00031-5

Intergovernmental Panel on Climate Change (IPCC). (2023). Technical Summary. In *Climate Change 2021 – The Physical Science Basis: Working Group I Contribution to the Sixth Assessment Report of the Intergovernmental Panel on Climate Change* (pp. 35-144). Cambridge: Cambridge University Press. doi:10.1017/9781009157896.002

Kirk-Davidoff, D. (2018). The greenhouse effect, aerosols, and climate change. *Green Chemistry,* 211-234. https://doi.org/10.1016/B978-0-12-809270-5.00009-1

Lassman, W., Pierce, J. R., Bangs, E. J., Sullivan, A. P., Ford, B., Mengistu Tsidu, G., Sherman, J. P., Collett, J. L., & Bililign, S. (2020). Using low-cost measurement systems to investigate air quality: A case study in Palapye, Botswana. *Atmosphere*, 11(6), 583. https://doi.org/10.3390/atmos11060583

Levy, R. C., Remer, L. A., Kleidman, R. G., Mattoo, S., Ichoku, C., Kahn, R., & Eck, T. F. (2010). Global evaluation of the Collection 5 MODIS dark-target aerosol products over land. *Atmospheric Chemistry and Physics*, *10*(21), 10399–10420. https://doi.org/10.5194/acp-10-10399-2010

Michalsky, J. J., Schlemmer, J., Berkheiser, W. E., Berndt, J. L., Harrison, L. B., Laulainen, N. S., Larson, N., & Barnard, J. J. (2001). Multiyear measurements of aerosol optical depth in the Atmospheric Radiation Measurement and Quantitative Links programs. *Journal of Geophysical Research*, *106*(D11), 12099–12107. https://doi.org/10.1029/2001jd900096

Myhre, G., Myhre, C. L., Samset, B. H. & Storelvmo, T. (2013) Aerosols and their relation to global climate and climate sensitivity. *Nature Education Knowledge* 4(5).

Pryor, S. C., Crippa, P., & Sullivan, R. C. (2015). Atmospheric chemistry. *Reference Module in Earth Systems and Environmental Sciences*. https://doi.org/10.1016/b978-0-12-409548-9.09177-6

Shaw, G. E. (1983), Sun photometry. *Bulletin of the American Meteorological Society.* 64(1), 4–11. https://doi.org/10.1175/1520-0477(1983)064<0004:SP>2.0.CO;2

Sherman, J. P., Gupta, P., Levy, R. C., & Sherman, P. J. (2016). An evaluation of MODIS-retrieved aerosol optical depth over a mountainous AERONET site in the southeastern US. *Aerosol and Air Quality Research*, *16*(12), 3243–3255. https://doi.org/10.4209/aaqr.2015.09.0568

Sherman, J. P., & McComiskey, A. (2018). Measurement-based climatology of aerosol direct radiative effect, its sensitivities, and uncertainties from a background southeast US site. *Atmospheric Chemistry and Physics*, *18*(6), 4131–4152. https://doi.org/10.5194/acp-18-4131-2018

Twomey, S. (1974). Pollution and the planetary albedo. *Atmospheric Environment (1967)*, *8*(12), 1251–1256. https://doi.org/10.1016/0004-6981(74)90004-3

Voiland, A. (2010). *Aerosols: Tiny particles, big impact*. NASA. https://earthobservatory.nasa.gov/features/Aerosols#:~:text=Key%20aerosol%20groups%20include%20sulfates

Wilmot, T. Y., Mallia, D. V., Hallar, A. G., & Lin, J. C. (2022). Wildfire plumes in the Western US are reaching greater heights and injecting more aerosols aloft as wildfire activity intensifies. *Scientific Reports*, *12*(1), 12400. https://doi.org/10.1038/s41598-022-16607-3

Young, A. T. (1994). Air mass and refraction. *Applied Optics*, *33*, 1108–1110. https://doi.org/10.1364/AO.33.001108

Appendix A

Rendering of the 3D Model Featuring the Instrument Housing and Optical Block

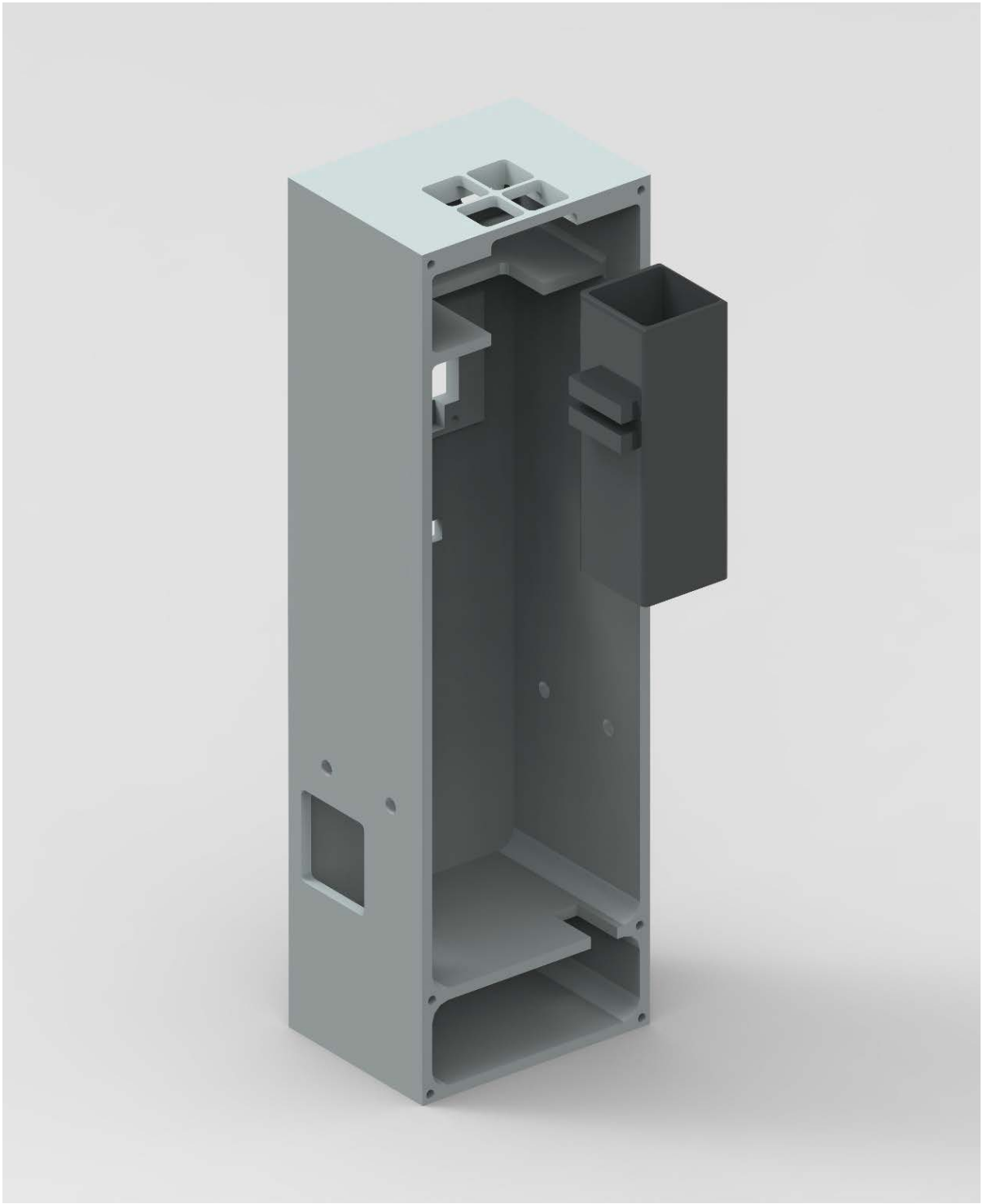

Appendix B

Gerber File Image of the Main Sunphotometer PCB

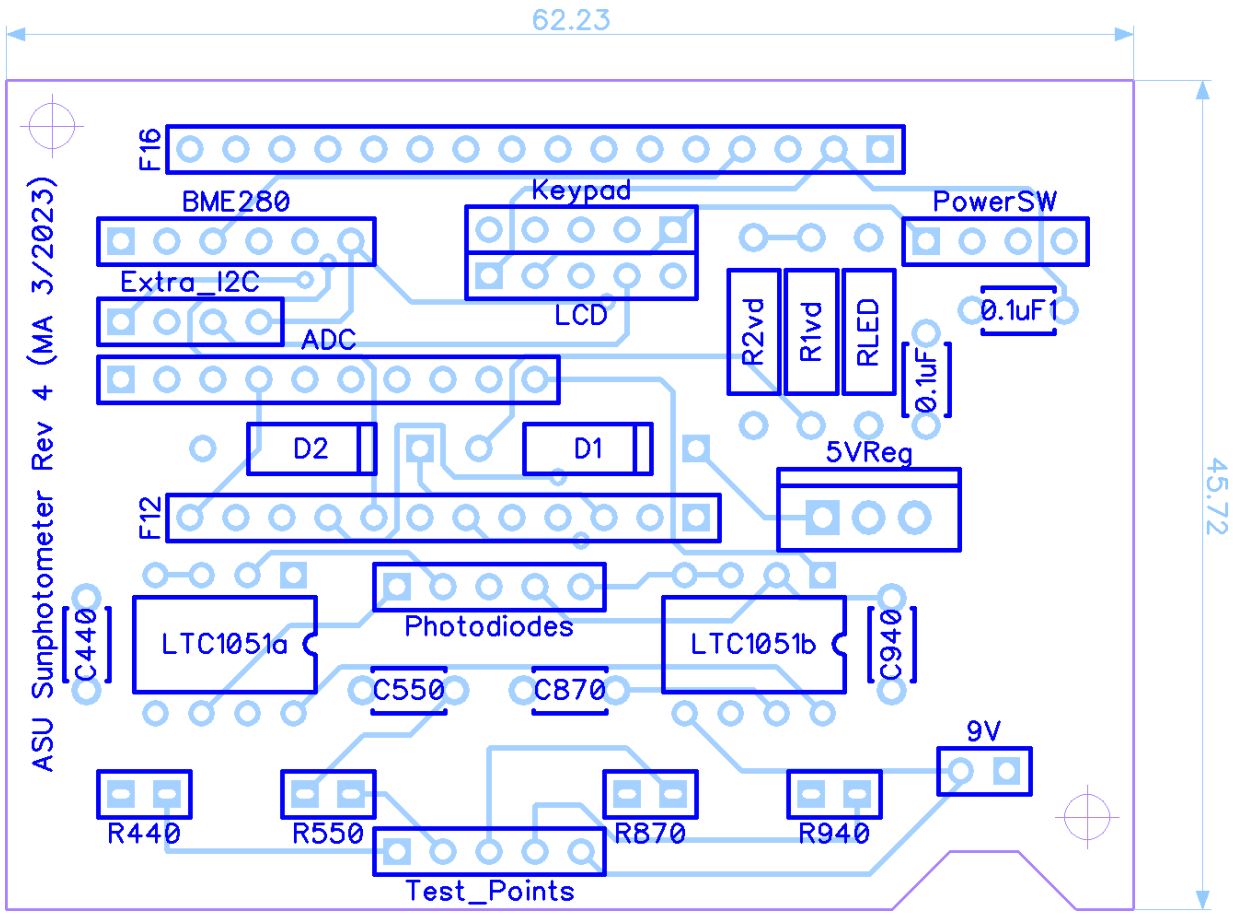

Appendix C

Table of Abbreviations Used Throughout This Thesis

Abbreviation	**Definition**
AOD	Aerosol Optical Depth
MODIS	NASA's Moderate Resolution Imaging Spectroradiometer
MISR	NASA's Multi-angle Imaging SpectroRadiometer
AERONET	NASA's Aerosol Robotic Network
GPS	Global Positioning System
CCN	Cloud condensation nuclei
IRE	Indirect Radiative Effect
DRE	Direct Radiative Effect
ERF	Effective Radiative Forcing
SSA	Single Scattering Albedo
AE	Angstrom exponent
PM2.5	Particulate matter less than 2.5 microns in diameter
GLOBE Network	Global Learning and Observations to Benefit the Environment
BIUST	Botswana International University of Science and Technology
NASAMAN	North American and Sub-Saharan Mountain Aerosol Network
OD	Optical Depth
PWV	Precipitable Water Vapor
CSV	Comma-Separated Values
PCB	Printed Circuit Board

Abbreviation	Definition
NMEA	National Marine Electronics Association
SPI	Serial Peripheral Interface
SD	Secure Digital
PC	Personal Computer
ASM	Algorithmic State Machine
IDE	Integrated Development Environment
LCD	Liquid Crystal Display
ADC	Analog-to-Digital Converter
RTC	Real-Time Clock
UTC	Coordinated Universal Time

Vita

Matthew Frederick Allen was born in Chapel Hill, North Carolina to Kimberlee Joyner and Michael Allen. He received his Bachelor of Science in Sustainable Technology from Appalachian State University in the spring of 2021. In the fall of 2021, Matthew enrolled in the Engineering Physics program at Appalachian State University. He was awarded his Master of Science degree in 2023.

Matthew worked throughout his undergraduate and graduate time at Appalachian State University, serving as Electrical Director of the Solar Electric Vehicle Team and teaching introductory physics labs.